J Nondestruct Eval (2017) 36:31
DOI 10.1007/s10921-017-0409-5

Characterization of Structural Noise Patterns and Echo Separation in the Time-Frequency Plane for Austenitic Stainless Steels

M. Khelil[1] · Jean-Hugh Thomas[2,3] · L. Simon[2] · R. El Guerjouma[2] · M. Boudraa[4]

Received: 4 May 2016 / Accepted: 20 March 2017

Abstract The aim of this study is to characterize the structural noise for a better flaw detection in heterogeneous materials (steels, weld, composites…) using ultrasonic waves. For this purpose, the continuous wavelet transform is applied to ultrasonic A-scan signals acquired using an ultrasonic non destructive testing (NDT) device. The time-scale representation provided, which highlights the temporal evolution of the spectral content of the A-scan signals, is relevant but can lead to misinterpretation. The problem is to identify if each pattern from the wavelet representation is due to the structural noise or the flaw. To solve this problem, a detection technique based on statistical significance testing in the time-scale plane is used. Information about the structural noise signals is injected into the decision process using an autoregressive model, which seems relevant according to the spectral content of the signal. The approach is tested on experimental signals, obtained by ultrasonic NDT of metallic materials (austenitic stainless steel) then on a weld in this steel and indeed enables to distinguish the components of the signal as flaw echoes, which differ from the structural noise.

Keywords Austenitic stainless steels · Structural noise · Flaw detection · Wavelet transform · Autoregressive model · Significance testing

✉ Jean-Hugh Thomas
jean-hugh.thomas@univ-lemans.fr

[1] Research Center in Industrial Technologies (CRTI), Bp 64, 16014 Cheraga, Algiers, Algeria

[2] LAUM, UMR CNRS 6613, Université du Maine, Av. O. Messiaen, 72085 Le Mans, France

[3] ENSIM, Université du Maine, Rue Aristote, 72085 Le Mans, France

[4] USTHB, Faculté d'Electronique, Bp 32, El Alia, 16111 Bab Ezzouar, Algiers, Algeria

1 Introduction

The austenitic stainless steels are used in various structures, in particular in the parts of the primary circuit within the nuclear reactors. It is then useful to monitor the state of these materials. Among the methods used to characterize the austenitic stainless steels' damages, non destructive testing (NDT) proved to be effective to detect various types of defects, whose presence could imperil industrial machines in process. Among NDT techniques, the ultrasonic inspection is very widespread used, which consists e.g. in emitting an ultrasonic pulse in the material and observing the possible echoes reflected by discontinuities. To carry out an ultrasonic acquisition, the controlled surface is scanned in a regular way by using a transmitting/receiving ultrasonic probe. In each scanned point, an ultrasonic shoot is carried out by the transmitter and the back wall echoes are recorded by the receiver. Thus for a given sensor, ultrasonic data are obtained in a four-dimensional space (see Fig. 1): (x, y) sensor space coordinates, (t) time spent by the echoes to reach the receiver, and (A) the amplitude of the echoes. The data resulting from an ultrasonic acquisition can be represented as a set of one-dimensional signals (A-scan), or as images (B-scan, C-scan, D-scan) allowing visualization and interpretation of the information provided by data acquisition. The B-scan representation [(y,z) plane] is a cross-sectional view of the test material's features, i.e., a line of A-scans. The C-scan [(y,x) plane] and D-scan [(x,z) plane] representations provide a plane view of the location and size of the test material features respectively for a specific depth (z) and a specific position (y).

The problem is often turned to the following questioning: How detecting damage from the observation of representations of the signal A-scan or the image B-scan? In addition, diagnosing the state of the austenitic stainless steels from

Published online: 03 April 2017

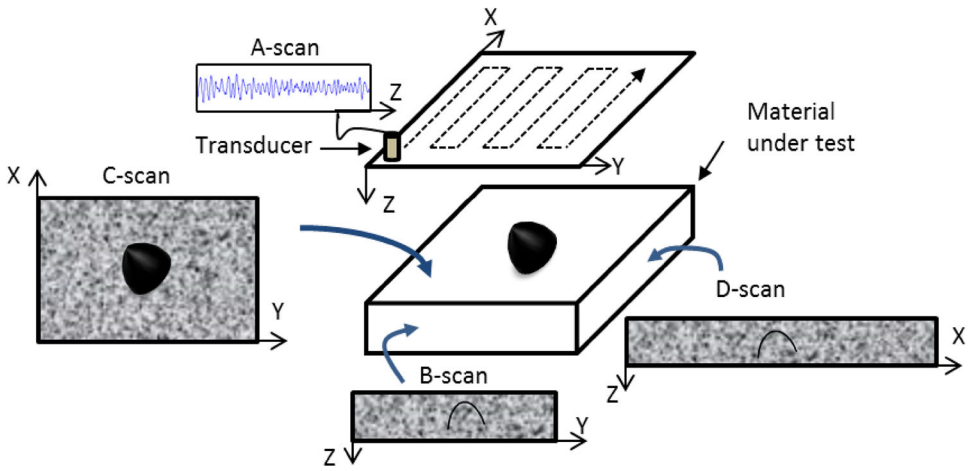

Fig. 1 Principal modes of representation (*A-scan*, *B-scan*, *C-scan*, *D-scan*) provided by NDT based on ultrasonic signal emission/reception

ultrasonic inspection is difficult due to the fact that ultrasonic waves generated into such materials cause the propagation of both coherent and incoherent waves. The incoherent waves called structural noise are due to scattering in the material, which is a complex phenomenon largely studied in the literature [1–3]. The presence of structural noise may hide the acoustic signature of the damage to detect. Thus, the ultrasonic NDT of the austenitic stainless steels is of major interest theoretically and experimentally. To be able to detect defects in this complex medium, many methods proposed are based on a representation of the signal [4,7,9–17]. It was demonstrated that the frequency is an important parameter to take into account. For instance Saniie et al. showed that the frequency content of the echoes scattered by grains depends on their size distribution and on the absorption conditions [4].

The echoes can then be characterized by estimating the maximum energy frequency defined as the frequency for which the power spectrum of the ultrasonic signal reaches the maximum value. The frequency evaluation of backscattered echoes using autoregressive (AR), Prony and Music methods [5,6] made the authors prefer the AR approach [7]. But very often the frequency representation of the A-scan signal is not sufficient. A time-frequency or time-scale representation [8] is necessary to improve the spatial accuracy of the defect localization. This representation also provides a better characterization of a waveform, exhibiting its time evolving frequency content [9]. Several signal processing tools as wavelet analysis, short time Fourier transform or Wigner–Ville distribution can lead to this representation [8]. Wavelets have been widely used in the field of NDT for this purpose, on 1D A-scan signals or on 2D signals like B-scan images. Robini et al. [10] use in particular a wavelet packet decomposition to highlight flaw information in B-scan images. From several sub-images obtained by the decomposition at various depths of a B-scan image, a thresholding procedure is implemented to select the most relevant coefficients. Then a denoised B-scan image is reconstructed.

Other operators as morphological filters were applied to B-scan images to remove the noise [11]. The wavelet-based reconstruction scheme is also applied to 1D A-scan signals for enhancing the signal-to-noise ratio (SNR) [12]. Either discrete wavelet transform (DWT) or continuous wavelet transform (CWT) is used in the study done by Kaya et al. [12]. The method first involves decomposing the signal into several frequency sub-bands. Then some coefficients are set to zero before reconstructing the time signal. Split spectrum processing (SSP) can also provide a filtered signal in the time domain by recombining elements separated in different spectral bands [13,14]. Kaya et al. [12] show that the DWT may lead to less relevant results than the CWT in the case of closely spaced multiple targets because of the constraint on the spectral processing range of the DWT.

In addition, the choice of the so-called mother wavelet has a significant influence on the results. In this way, Oruklu et al. [15] compare several mother wavelets to implement the DWT on experimental and simulated data. They conclude that the Battle–Lemarie wavelet with six vanishing moments and the Vaidyanathan wavelet with 24 vanishing moments provide a flaw-to-clutter ratio enhancement of 5–12 dB when the measured flaw-to-clutter ratio is 0 dB or less. It is also of major interest to use the CWT in order to build a specific wavelet well-suited to the experimental ultrasonic signals. Abbate et al. [16] design a mother wavelet from the acoustic wave reflected by a flaw, and thus take into account the frequency response of the transducer. They apply the CWT successfully to steel samples with simulated flaws with different dimensions. Other models as Gaussian chirplet have been proposed for characterizing ultrasonic backscattered echoes [17].

Therefore, according to the literature, wavelet analysis can be used for characterizing the echoes, extracting a signature, which links the time occurrences to their spectral content. The analysis provides finally a data representation, which will be considered by some experts to take a decision. Then the representation can be enhanced through different strategies: one approach consists in filtering the noise that does

not seem to correspond to the useful signal with the risk of deleting relevant information [10–12]. The other approach is searching a filter more adapted to the echoes to recognize [16,17]. But after all, whatever the approach, it is necessary to automatically take the decision from the representation. The method presented in this paper works on the time-scale plane representation of the experimental data. It is based on separating, in this plane, the pattern of the flaw or of the weld echo from that of the background grain noise. The separation algorithm implements hypothesis testing decision. Other studies applying statistical tests provide satisfactory results to detect welds badly oriented in relation to the ultrasonic beam [18] for instance or to detect flaws using the Bayes classification from frequencies, (some of them due to defects, the others to the materials grains) [19].

Our approach consists in injecting a prior knowledge on the frequency content of the structural noise in the hypothesis testing. This prior knowledge allows us to modify the scalogram and then the representation to highlight the appearance of a flaw or weld echo. Hypothesis testing is carried out to determine the best hypothesis between: "pattern corresponding to structural noise is present" (H_0) versus "pattern revealing something else is present such as the signature of a flaw" (H_1). As a consequence, hypothesis testing requires structural noise characterization. In this paper, the power spectral density (PSD) estimates the spectral content of ultrasonic signals revealing a structural noise, using an autoregressive model. The decision making of this study is based on works related to geophysical research [20–22], which show that the approach is well adapted to separate the signatures in the time-frequency plane computed from sea surface temperature data. In this paper, the aim is to separate the signature of the structural noise from other signatures such as flaws. The material (austenitic stainless steel) and the ultrasonic signals studied are described in the second section. The approach used which consists in representing A-scan signals in the time-scale plane by wavelet analysis, characterizing structural noise and detecting flaws in the material is reported in the third section. Experimental results are reported in the last section.

2 Materials and Ultrasonic Signals

The approach is tested on experimental signals obtained by an ultrasonic scan of metallic materials: a rolled austenitic stainless steel 316L (Material A), and a similar steel 316L with a welding zone (Material B). Two side-drilled holes were machined in the bottom right of the material A. This sample is tested using a transversal wave with a 60° beam angle in the (y,z) plane with respect to the vertical axis. The choice of this inspection angle is twofold: It allows one to detect tilted flaws and only transverse waves are refracted

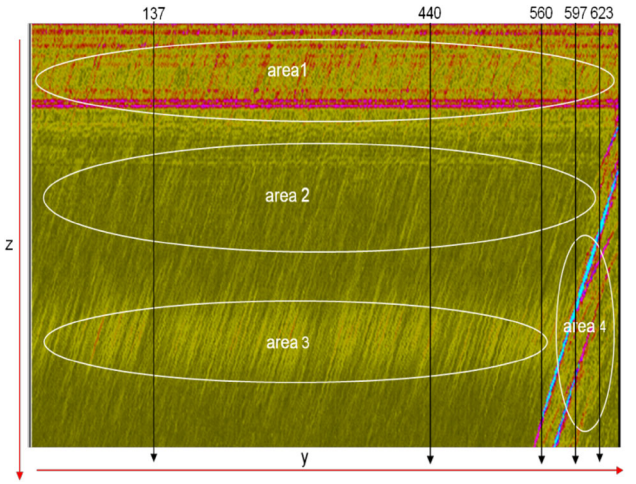

Fig. 2 B-scan image of material A highlighting a rebound echo (*area 1*), structural noise (*area 2*), strong structural noise (*area 3*) and defect echoes (*area 4*)

into the material, which makes the diagnosis more workable. The transducer used for this control has a 2 MHz central frequency. The signals are acquired with a sampling rate of 50 MHz. For this test, 643 A-scans are recorded. Figure 2 shows the B-scan image obtained from this material, in the plane (y,z): axis z represents the depth of the material and axis y represents a set of A-scan signals collected step by step over the width of the material. In this image, four areas are distinguishable: Area 1 representing echoes of rebounds due to the mounting-block of the transducer, area 2 representing a structural noise in the base metal, area 3 representing a strong raising noise and area 4 representing echoes of defects. These areas were identified by experts of EDF who also made artificial flaws, visible in area 4 of the B-scan as two main oblique lines.

Two A-scan signals, A-scan no. 440, (see Fig. 3) and A-scan no. 597 (see Fig. 4) are extracted from the positions marked in Fig. 2. The first signal is without any defect and the second one crosses two defects (see area 4 in Fig. 2). Both signals are corrupted by the same structural noise (see area 2 in Fig. 2). The second part of the signals (at the bottom of the B-scan image) shows a more energetic structural noise (see area 3 in Fig. 2) than the first part. A rebound echo can be observed (see the horizontal thick line in area 1 in Fig. 2) due to the transducer mounting-block in [3–5 μs] of the A-scan signals (see also Figs. 3, 4).

The material B is a mock-up of 316L industrial austenitic stainless steel weld manufactured using an arc welding process with coated electrodes. The welding position is flat position. The electrode diameter is 4 mm and the welding speed is 170 mm/min. The welding energy is 0.8 kJ/mm. The metal weld under investigation has a V-shaped chamfer filled by the steel material AISI 316L. The welded zone is 50 mm

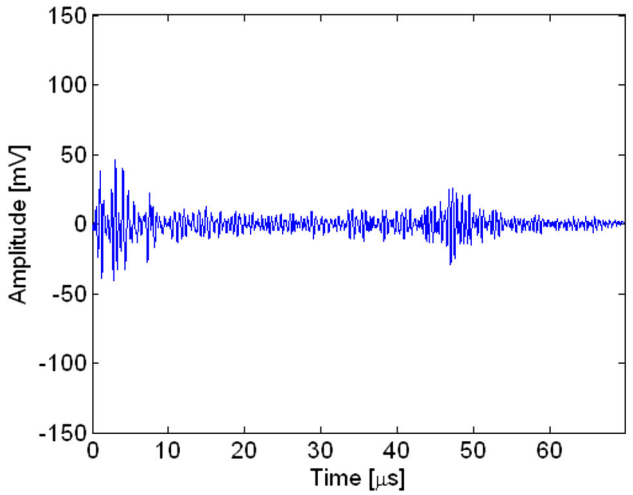

Fig. 3 Ultrasonic signal A-scan no. 440 at the position marked in Fig. 2. According to the zones identified by experts from the B-scan of Fig. 2, area 1 (rebound due to the transducer installation) is in [1–8 μs], area 2 (structural noise) in [16–34 μs] and area 3 (strong raising noise) in [37–60 μs]

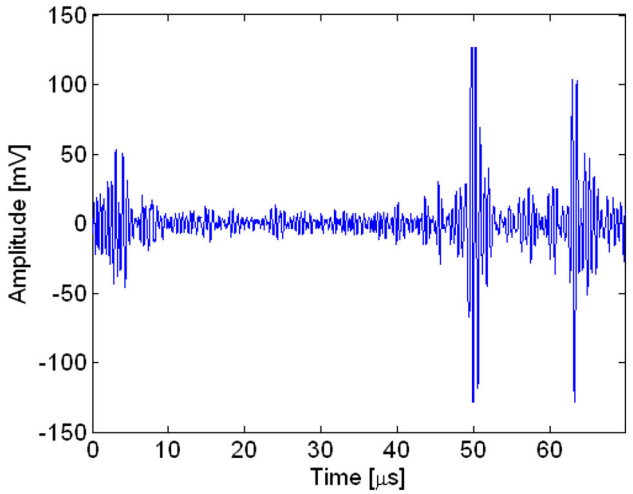

Fig. 4 Ultrasonic signal A-scan no. 597 at the position marked in Fig. 2. According to the zones identified by experts from the B-scan of Fig. 2, area 1 (rebound due to the transducer installation) is in [1–8 μs], area 2 (structural noise) in [18–20 μs] and area 4 (flaws) in [40–66 μs]

thick, the top width is 150 mm and the weld root is 50 mm. The length of the welding zone is supposed to be large enough to obtain elongated parallel grains. The grain orientation is from 15° to 20° with respect to the vertical axis.

The material B is tested using a transversal wave with a 45° beam angle in the (y,z) plane with respect to the vertical axis. In the presence of welds, because of the grain structure, the deviation of the ultrasonic beam within the weld material may cause difficulties in locating defects [23]. From the knowledge of the grain orientation of the weld studied, the angle of refraction of 45° gives optimal results with a transducer producing longitudinal waves. The transducer used for

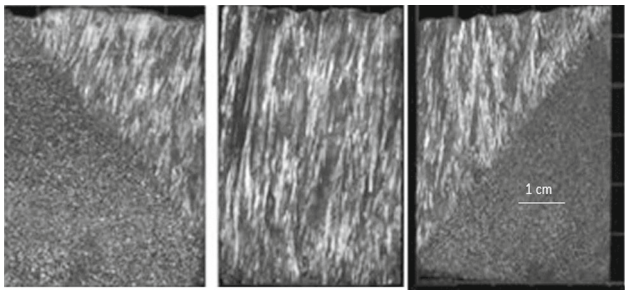

Fig. 5 Stainless steel D703 weld macrographs [24]

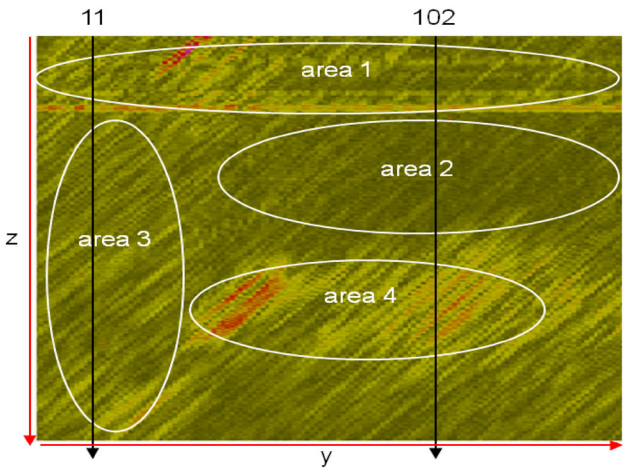

Fig. 6 B-scan image of material B highlighting a rebound echo (*area 1*), the welding zone (*area 2*), structural noise (*area 3*) and strong structural noise (*area 4*)

this control has a 2 MHz central frequency. The signals are acquired at a 20 MHz sampling rate. For this test, 184 A-scans are recorded. This sample contains a D703 weld [24] which is characterized by lengthened grains expanded through several passes. The macrographs in Fig. 5 show the different grain structures of the material and highlight the boundaries between the weld and the surrounding structure. They are used to describe accurately the sample and then validate the diagnosis provided by the method.

Figure 6 shows the B-scan image obtained from this material in the (y,z) plane. In this image, four areas are distinguishable, area 1 representing a rebound echo due to the transducer mounting-block, area 2 representing the welding zone, area 3 representing structural noise in the base metal and area 4 representing strong raising noise echoes due to the reflections of the transverse waves at the bottom of the weld at the weld-surrounding structure interface.

For this study, two particular A-scan signals are chosen: one (A-scan no. 11 in Fig. 7) related to the base metal propagation (area 3), and the other (A-scan no. 102 in Fig. 8) to the weld (area 2). The noise embedded in the A-scan no. 11 signal is strong while the noise level in the weld area is relatively weak in A-scan no. 102 signal. Rebound echoes (area 1) are present in the first samples of both signals.

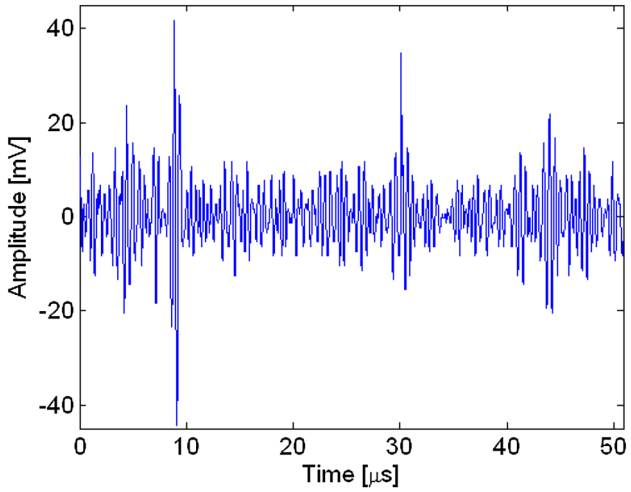

Fig. 7 Ultrasonic signal A-scan no. 11 at the position marked in Fig. 6. According to the zones identified by experts from the B-scan of Fig. 6, area 1 (rebound due to the transducer installation) is in [5–11 μs] and area 3 (structural noise) in [13–50 μs]

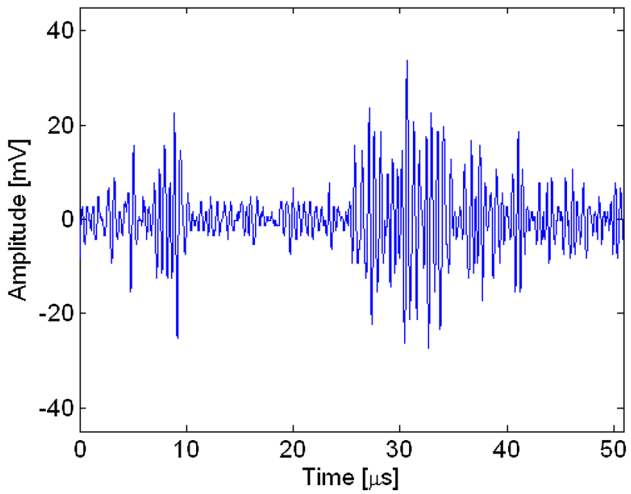

Fig. 8 Ultrasonic signal A-scan no. 102 at the position marked in Fig. 6. According to the zones identified by experts from the B-scan of Fig. 6, area 1 (rebound due to the transducer installation) is in [5–11 μs], area 2 (structural noise) in [12–19 μs] and area 4 (strong structural noise) in [22–43 μs]

The aim of the technique proposed in the next section is to underline the parts of the A-scan signals, which differ from the characteristics of the structural noise.

3 Method

3.1 Principle

The starting point of the study, which is described by a synoptic panel shown in Fig. 9, is the time-scale representation of an A-scan signal.

This representation is obtained by performing the CWT of the signal in order to represent its scalogram which may be difficult to interpret (see Fig. 10).

Then, the aim is to provide quantitative information to make the interpretation of each pattern (composed of several high coefficients of the scalogram $|W_x(\tau, s)|^2$) easier and to know if these patterns correspond to the structural noise or to some flaws. For this purpose, hypothesis testing is carried out. From different patterns extracted from the scalogram of an A-scan signal, the goal is to decide between the two following hypotheses:

- the pattern corresponds to the structural noise (H_0),
- the pattern indicates something else such as the signature of a flaw for example (H_1).

Thus hypothesis testing requires to characterize the structural noise. The approach used is based on the study of the experimental PSD of some ultrasonic signals highlighting a structural noise according to macrographs or experts. The PSD can also be computed using an autoregressive (AR) model [5].

3.2 Time-Scale or Time-Frequency Representation

The CWT $W_x(\tau, s)$ of the signal $x(t)$ consists in projecting $x(t)$ onto a basis designed from scaled and translated versions $\psi_{\tau,s}(t)$ of the mother wavelet $\psi_{(t)}$ such as

$$W_x(\tau, s) = \int_{-\infty}^{+\infty} x(t)\, \psi^*_{\tau,s}(t)\, dt, \tag{1}$$

where $\psi_{\tau,s}(t)$ is considered as the analyzing wavelet,

$$\psi_{\tau,s}(t) = \frac{1}{\sqrt{s}} \psi\left(\frac{t-\tau}{s}\right), \tag{2}$$

s the scale parameter and τ the time localization parameter [8]. * denotes the complex conjugate operator. The use of several scales s in the wavelet transform enables to obtain a time-scale representation of the signal $x(t)$ called scalogram defined as

$$S_{W,\psi}(\tau, s) = |W_x(\tau, s)|^2 . \tag{3}$$

Among the analyzing wavelets usually employed in signal processing, the so-called Morlet wavelet is chosen in this study, because of its characteristic parameters α_0 and ω_0 which may easily be suited to the recorded ultrasonic echoes. Figure 11 highlights both real and imaginary parts of the Morlet wavelet for $\alpha_0 = 1$ and $\omega_0 = 6$ rad s^{-1}. The Morlet wavelet is defined by [8]:

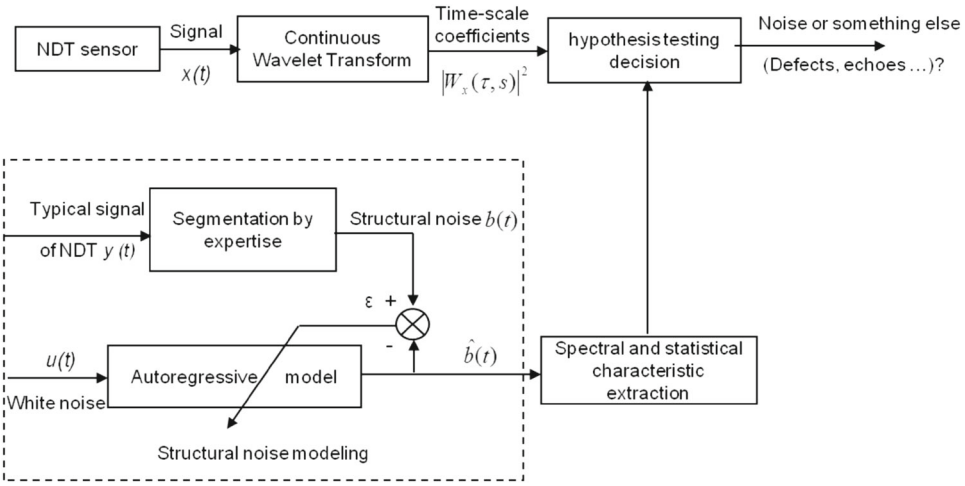

Fig. 9 Synoptic panel of the analysis method proposed

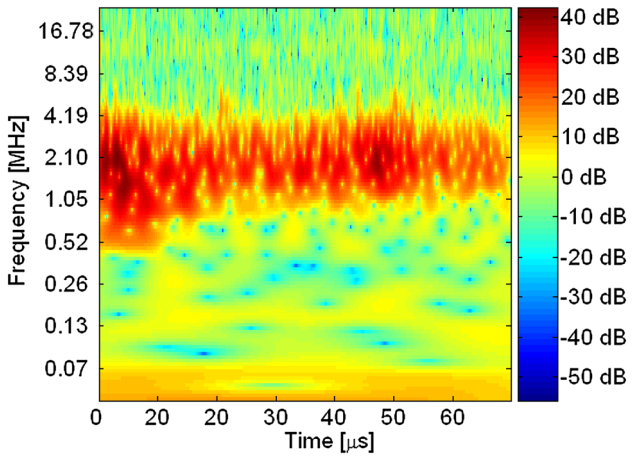

Fig. 10 A-scan no. 440 signal scalogram in dB

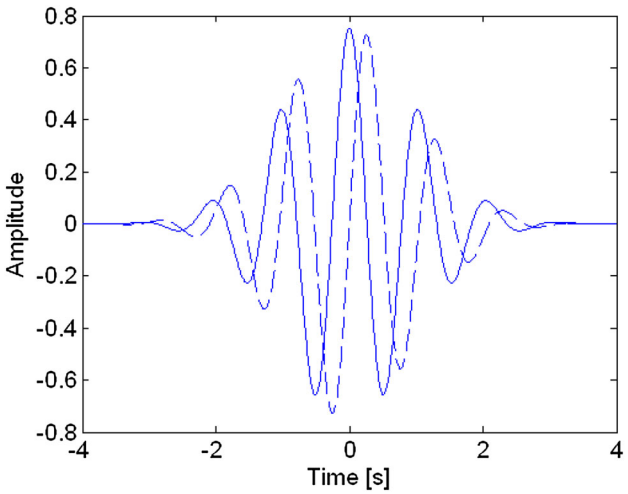

Fig. 11 Real part (*solid line*) and imaginary part (*dashed line*) of the Morlet mother wavelet for $\omega_0 = 6\,\mathrm{rad\,s^{-1}}$ and $\alpha_0 = 1$

$$\psi(t) = \pi^{-1/4}\sqrt{\alpha_0}\, e^{j\omega_0 t} e^{-\alpha_0^2 t^2/2}, \tag{4}$$

where α_0 fits the decrease in amplitude of the wavelet and where the pulsation ω_0 sets the period of the oscillations. A choice of $\alpha_0 = 1$ and $\omega_0 = 6\,\mathrm{rad\,s^{-1}}$ yields an acceptable wavelet in the sense that the wavelet admissibility condition [8,25] is almost fulfilled. The term $\pi^{-1/4}\sqrt{\alpha_0}$ standardizes the energy of the wavelet so that

$$\int_{-\infty}^{+\infty} |\psi(t)|^2\, dt = 1. \tag{5}$$

The Morlet mother wavelet (with a scale $s = 1$) corresponds to a band-pass filter centered on the frequency $f_0 = \omega_0/2\pi$. Here is $f_0 = 0.95\,\mathrm{Hz}$ for $\omega_0 = 6\,\mathrm{rad\,s^{-1}}$. The Fourier transform $\Psi_s(f)$ of the analyzing wavelet $\psi_{0,s}(t)$ corresponds to a band-pass filter centered on the frequency $f_s = f_0/s = \omega_0/2\pi s$ (see Fig. 12). This frequency property establishes the rule to match up a time-scale plane (t, s) with a time-frequency plane (t, f_s). The continuous wavelet transform computation is carried out via the software [26].

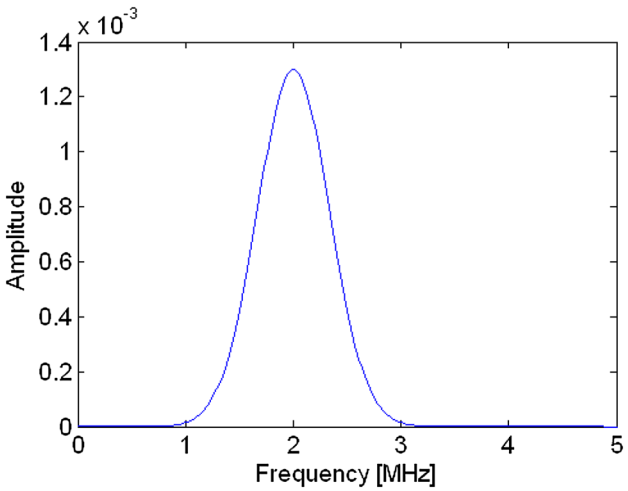

Fig. 12 Morlet wavelet analyzing spectrum for $\omega_0 = 6\,\mathrm{rad\,s^{-1}}$ and $\alpha_0 = 1$ obtained by contraction of the mother wavelet at scale $s = 4.77 \times 10^{-7}$ corresponding to frequency $f_s = 2\,\mathrm{MHz}$

3.3 Autoregressive Modeling

By autoregressive modeling, it is possible to synthesize a signal $\hat{b}(t)$ whose statistical properties (specifically the autocorrelation function) are similar to that of a sample of the structural noise $b(t)$ [5]. It consists in filtering a white noise with variance σ^2, with an autoregressive filter composed of p coefficients $a_i (i = [1, p])$. The filter coefficients as well as the white noise variance are obtained by resolving the Yule–Walker equation system [5]. Then the synthesized signal $\hat{b}(t)$ discretised with sampling period T_s is written at time nT_s

$$\hat{b}\,(nT_s) = u\,(nT_s) - \sum_{i=1}^{p} a_i \hat{b}\,((n-i)\,T_s) \tag{6}$$

where $u(nT_s)$ is a white noise with variance σ^2. One of the major interests of this model is that $S_{\hat{b}}(f)$ the PSD for frequency f of the autoregressive signal $\hat{b}\,(t)$ is known analytically:

$$S_{\hat{b}}(f) = \frac{\sigma^2 T_s}{\left|1 + \sum_{i=1}^{p} a_i e^{-2j\pi f i T_s}\right|^2}. \tag{7}$$

Thus this PSD highlights the frequency content of the structural noise. The main difficulty of autoregressive modeling is the choice of the order p of the model. However, some criterion $J\,(p)$ can be used as the Final Prediction Error $FPE\,(p)$ [see Eq. (8)] or the Akaike's Information Criterion $AIC\,(p)$ [see Eq. (9)] to estimate the number $\hat{p}$ of filter coefficients [5]:

$$J\,(p) = FPE\,(p) = \frac{N+p}{N-p}\sigma_p^2, \tag{8}$$

$$J\,(p) = AIC\,(p) = 2p + N \log \sigma_p^2. \tag{9}$$

N is the number of samples of the signal and σ_p^2 is the driving white noise variance in the case of an AR model of order p. The estimated order $\hat{p}$ of the model corresponds in general to the minimal value of the criterion such as

$$\hat{p} = Arg \min_p J\,(p)\,. \tag{10}$$

3.4 Hypothesis Testing

Hypothesis testing is introduced to find out whether a pattern of the time-scale plane corresponds or not to the structural noise. In our study, the amplitudes of the signal $x(t)$ representative of structural noise are distributed according to a Gaussian probability density function (PDF), which is illustrated in Fig. 14. It is established that the real part $R_e(X(f))$ and the imaginary part $I_m(X(f))$ of the Fourier transform $X(f)$ of such a signal $x(t)$ are also distributed according to a Gaussian PDF [21,27]. Since the square of a Gaussian distributed random variable is distributed according to a chi-squared PDF χ_1^2 with one degree of freedom, the square of the spectrum modulus of $x(t)$ is deduced to have a chi-squared PDF χ_2^2 with two degrees of freedom. This statement was demonstrated [28] and assessed [29] in the case of the spectrogram representation of data. Let us consider a vertical section $V_{n_1}(s) = |W_x(n_1, s)|^2$ of the scalogram $|W_x(n, s)|^2$ at time n_1. $V_{n_1}(s)$ corresponds to the frequency content of the signal $x(n_1 T_s)$ and thus can be seen as its instantaneous spectral power density. This assumption can be validated as in [21], by generating L autoregressive models of structural noise, by computing their scalograms, by isolating one vertical section $V_{n_1}^l(s)$(with $l = 1, L$) per scalogram and by finding out the average of L sections $V_{n_1}^l(s)$ $(l = 1, L)$ for each scale s or each frequency. When this average corresponds to the theoretical PSD [Eq. (7)] then one can say that the scalogram $|W(n, s)|^2$, just as $|X(f)|^2$, is distributed according to a chi-squared PDF χ_2^2 with two degrees of freedom.

If the signal $x(t)$ is white noise with variance σ_0^2, the decorrelation of the samples in the frequency domain implies

$$E\left[X(f)\,X^*\left(f'\right)\right] = \sigma_0^2 \delta\left(f - f'\right), \tag{11}$$

where $E[\,]$ indicates the statistical expectation and δ the Dirac impulse. f and f' denote frequencies.

Using the two following properties [8] of the continuous wavelet transform,

$$W_x(\tau, s) = \int_{-\infty}^{+\infty} X(f)\,\Psi_s(f)\,e^{2j\pi f\tau} df, \tag{12}$$

$$\int_{-\infty}^{+\infty} |\Psi_s(f)|^2\,df = 1, \tag{13}$$

involving the Fourier transform $X(f)$ of the signal $x(t)$ and the Fourier transform $\Psi_s(f)$ of the analyzing wavelet $\psi_{0,s}(t)$, the scalogram expectation of a white noise with variance σ_0^2 follows:

$$E\left[|W_x(\tau, s)|^2\right] = \sigma_0^2 \int_{-\infty}^{+\infty} |\Psi_s(f)|^2\,df = \sigma_0^2. \tag{14}$$

In this case the scalogram is distributed according to a chi-squared PDF χ_2^2 with two degrees of freedom:

$$\frac{|W_x(\tau, s)|^2}{\frac{1}{2}\sigma_0^2} \rightarrow \chi_2^2, \tag{15}$$

where 1/2 comes from the freedom degrees of the PDF and where " $\rightarrow$" means: is distributed according to.

When the signal $x(t)$ is not a white noise, but a colored noise, Eq. (15) is rewritten as

$$\frac{|W_x(\tau,s)|^2}{\frac{1}{2}P_s} \rightarrow \chi_2^2, \tag{16}$$

where P_s corresponds to the frequency content (PSD) of the signal at frequency $k/(NT_s)$. This frequency is associated to the scale s such as $k/(NT_s) = f_0/s$. According to Eq. (7),

$$P_s = S_{\hat{b}}(k/NT_s) = \frac{\sigma^2 T_s}{\left|1+\sum_{i=1}^{p} a_i e^{-2j\pi ki/N}\right|^2}. \tag{17}$$

Let $g(z)$ be the PDF of a random variable Z distributed according to a chi-squared PDF χ_2^2 with two degrees of freedom. The right-tail probability Q for the χ_2^2 random variable is defined as

$$Q_{\chi_2^2}(\gamma) = \int_{\gamma}^{+\infty} g(z)dz = \text{Prob}(Z > \gamma) = \alpha. \tag{18}$$

Here, $Q_{\chi_2^2}(\gamma)$is also referred to as the probability of false alarm since deciding (H_1) that a defect appears in the signal when the signal should be only structural noise (H_0) can be thought of as a false alarm. From (16), a defect in the signal is highlighted if the quantity $2|W_x(n,s)|^2/P_s$ is above the threshold γ, that is

$$\text{Prob}\left(\frac{|W_x(\tau,s)|^2}{\frac{1}{2}P_s} > \gamma\right) = \alpha, \tag{19}$$

and then,

$$\text{Prob}\left(\frac{|W_x(\tau,s)|^2}{\frac{1}{2}\gamma P_s} > 1\right) = \alpha. \tag{20}$$

Thus the decision rule depends on the quantity

$$G(\tau,s) = \frac{|W_x(\tau,s)|^2}{\frac{1}{2}\gamma P_s}. \tag{21}$$

- let us decide H_1 if $G(\tau,s) > 1$: a defect appears in the signal.
- let us decide H_0 if $G(\tau,s) \leq 1$: the signal is a structural noise.

This decision is made at each point of the time-frequency plane with a confidence interval $1-\alpha$. Therefore, it is necessary to choose the probability of false alarm α to apply the method, which is equivalent to set the threshold γ. Indeed, the quantity $G(\tau,s)$ depends on the data (the scalogram $|W(n,s)|^2$ of the A-scan considered), on prior knowledge of the frequency content of the structural noise (P_s) and on the threshold γ. The only parameter to tune is then this threshold γ. This can be advantageously done, as a calibration process, on a material with artificial flaws whose positions are known or from discussions with experts to adjust the sensitivity in such a way that actual defects could be detected.

4 Results

The approach is tested on experimental A-scan signals obtained by ultrasonic inspection of a metallic material, an Austenitic Stainless Steel (A) and a weld in this steel (B).

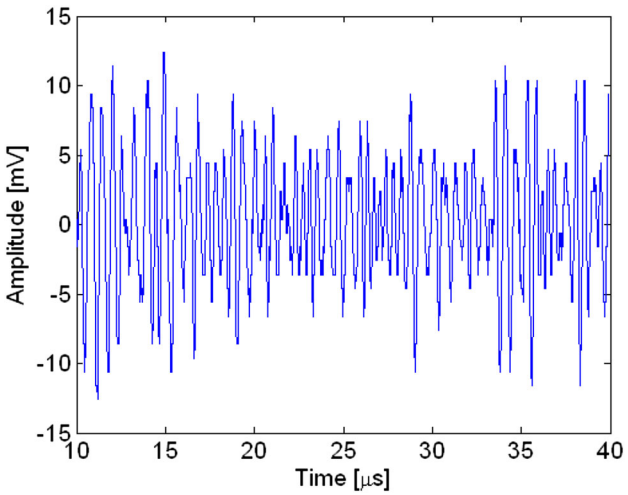

Fig. 13 Typical structural noise signal extracted from the B-scan image (area 2) in Fig. 2

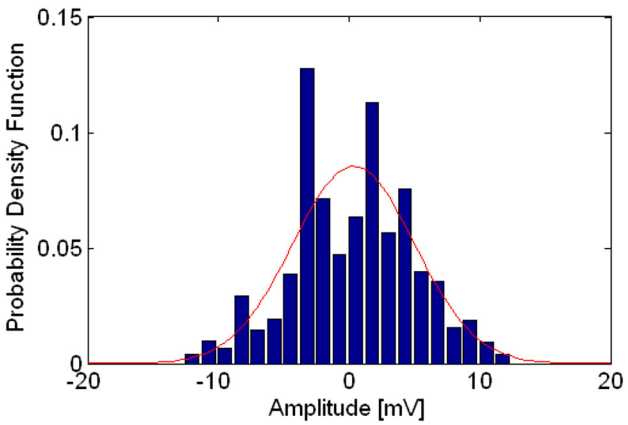

Fig. 14 Experimental amplitude distribution of the structural noise signal in Fig. 13 and the Gaussian function obtained from the mean and the variance of the noise

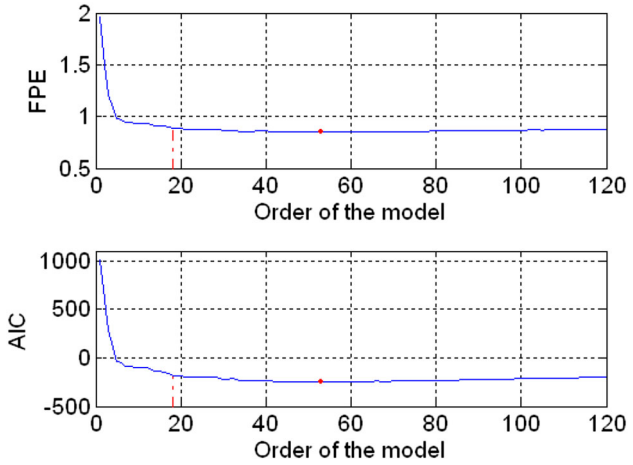

Fig. 15 Choice of the order of the autoregressive model from criteria final prediction error (FPE) and Akaike's information criterion (AIC) defined in Eqs. (8) and (9). The *vertical dash-dotted lines* indicate the order chosen for the study ($p = 18$) and the *point marks* the order corresponding to the minima of the criteria ($p = 53$)

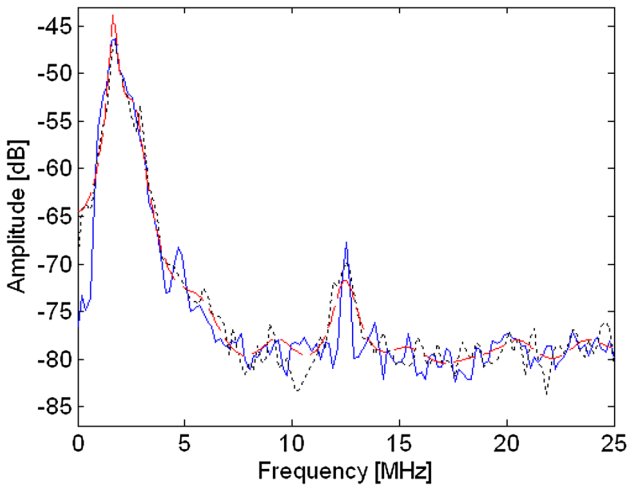

Fig. 16 Structural noise in the frequency domain: experimental PSD (dB) of the structural noise signal in Fig. 2 (*solid line*), experimental PSD of the AR signal of order 18 (*dotted line*) and theoretical PSD of $\hat{b}(t)$ according to Eq. (7) with the filter coefficients provided by the AR model (*dash-dotted line*)

4.1 Structural Noise Autoregressive Modeling

A typical signal of structural noise $b(t)$ (see Fig. 13) is extracted from the B-scan image (see Fig. 2). This signal has a normal PDF (see Fig. 14), which is checked by the test of Shapiro and Wilk [30]. The normal PDF of the full zone of structural noise (area 2) has also been verified. The signal is then modeled using an autoregressive process. The order of the model is estimated by the Akaike's criteria *FPE* [Eq. (8)] and *AIC* [Eq. (9)], represented in Fig. 15. The curves obtained show a quick decrease of the criteria according to the order of the model. The minimum of the two functions is

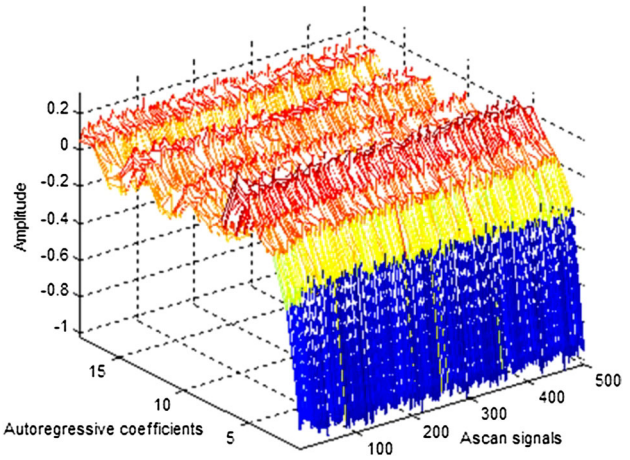

Fig. 17 Autoregressive coefficients of the structural noise signals extracted in the second area in Fig. 2

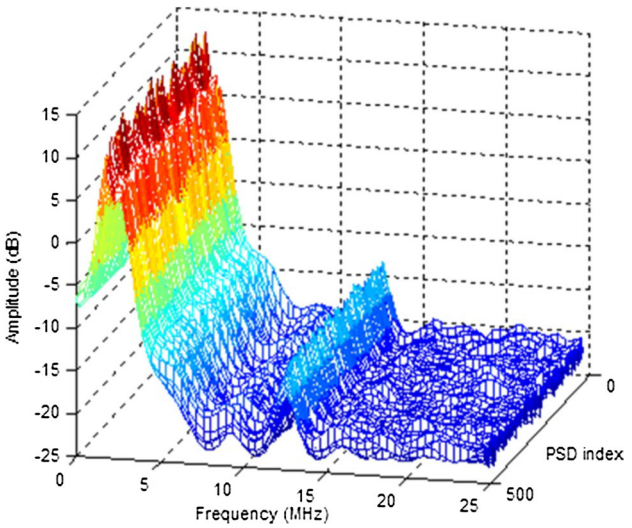

Fig. 18 Theoretical power spectral densities of the structural noise signals calculated from the coefficients in Fig.17 using Eq. (7)

obtained for order $p = 53$. However, it is to be noticed that the difference of both criteria between the orders 18 and 53 remains lower than 6% of the variation range of the criteria. It means that for orders greater than $p = 18$, the decrease of the criteria is not significant. Then for the study, $p = 18$ has been chosen as the order of the AR model, involving less computation than for $p = 53$.

Figure 16 shows the theoretical PSD obtained by Eq. (7) or (17), that of the AR signal $\hat{b}(t)$ of order 18 and that of the structural noise $b(t)$ represented in Fig. 13, both computed by the Welch periodogram [31,32].

Figure 16 shows clearly a relevant modeling of the structural noise through the comparison between the Power Spectrum Densities of the structural noise signal and the AR signal. The choice of a signal representative of the structural noise has a small influence on the results as soon as the signal

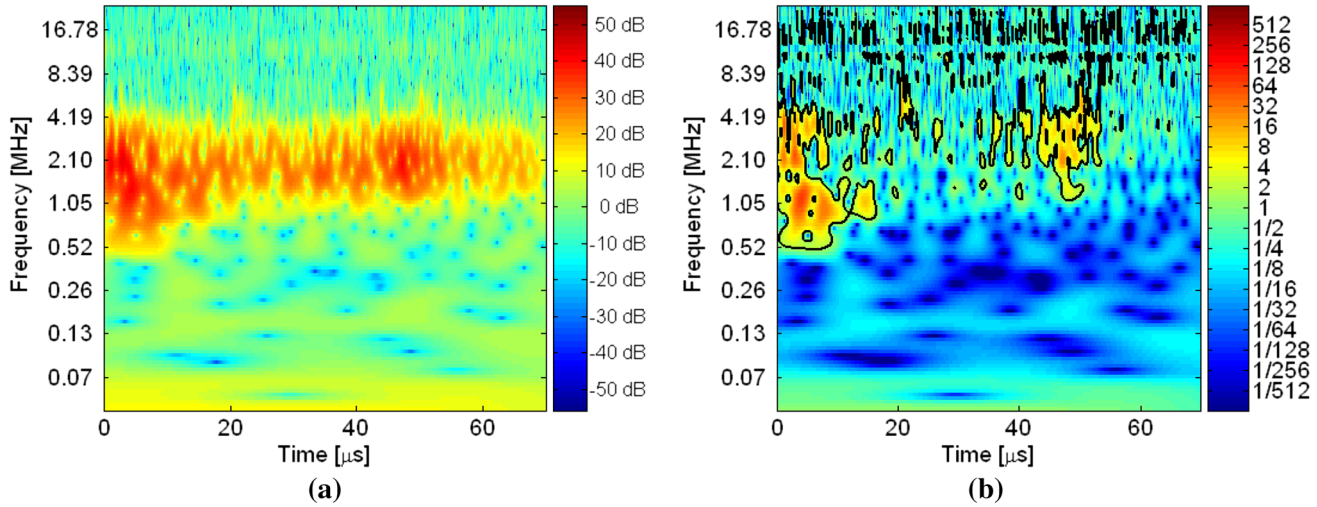

Fig. 19 Time-frequency representations of A-scan no. 440: **a** scalogram, **b** scalogram modified according to Eq. (21)

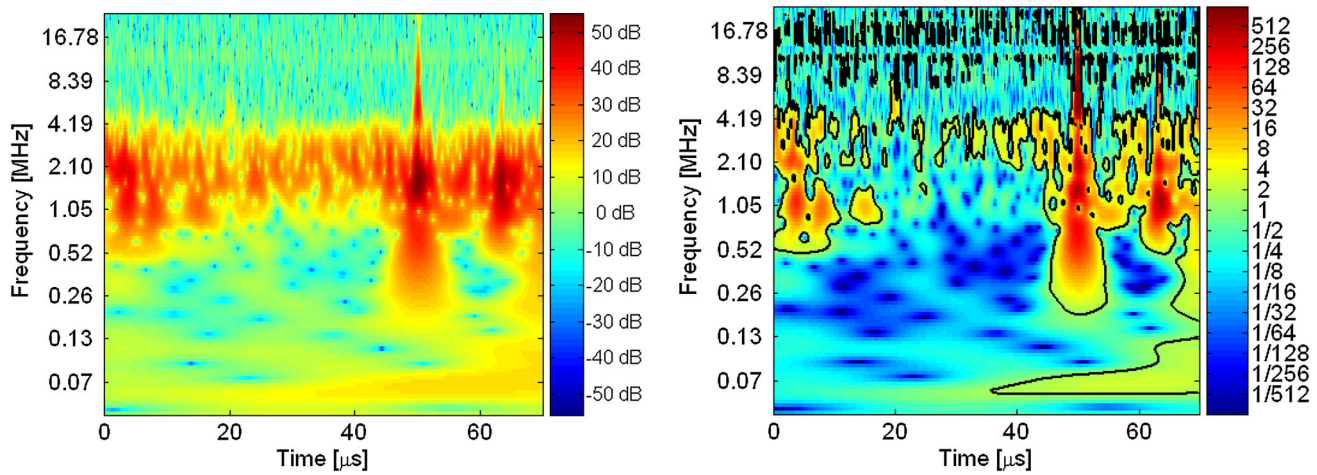

Fig. 20 Time-frequency representations of A-scan no. 597: **a** scalogram, **b** scalogram modified according to Eq. (21)

is extracted from the noise area (area 2) of the B-scan representation (see Fig. 2). To validate this point, several structural noise signals have been extracted from this area. From their 18-order AR models, the PSDs have been computed. Figure 17 shows the AR coefficients of each A-scan signal. Figure 18 represents the theoretical PSD of the synthesized signals computed from the coefficients in Fig. 17.

The theoretical PSDs are similar and the AR model coefficients are stable. The use of an average noise obtained by the mean calculation of the A-scan signals in the noise area or the use of an autoregressive signal whose coefficients are obtained by the mean calculation of the coefficients in Fig. 17 leads to very similar time-frequency representations.

4.2 Decision in the Time-Frequency Plane

4.2.1 Material A

The purpose of this part is to show the results obtained for the A-scan signals, extracted from the B-scan image (see Fig. 2). The scalogram modified according to Eq. (21) of signal A-scan no. 440 (see Fig. 3) is presented in Fig. 19b near the original scalogram in Fig. 19a. A similar representation for the scalograms of signal A-scan no. 597 (see Fig. 4) is given in Fig. 20. It is important to notice that keeping the highest contour levels of the scalograms in Figs. 19a and 20a cannot provide the scalograms in Figs. 19b and 20b. Indeed the decision process depends on the frequency considered.

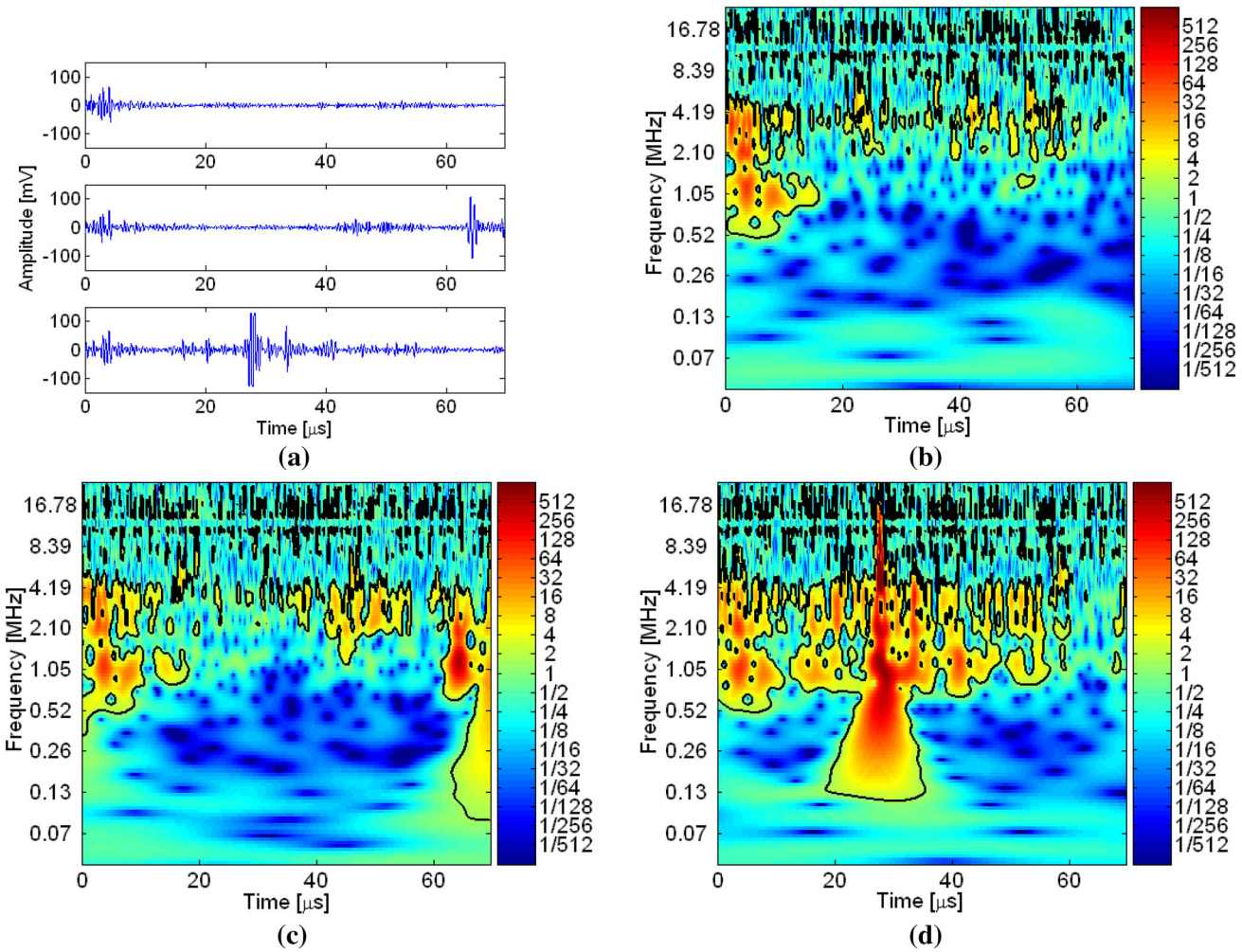

Fig. 21 Time-frequency representations of other A-scans: modified scalograms of **b** A-scan no. 137 [**a** top], **c** A-scan no. 560 [**a** middle] and **d** A-scan no. 623 [**a** bottom]

The contours in Figs. 19b and 20b correspond to the area where the modified scalogram $G(\tau, s)$ is above 1 [Eq. (21)]. According to hypothesis testing as described in Sect. 3.4, these contours indicate the areas where the signal cannot be considered as a structural noise (hypothesis H_1), with a confidence interval of 95% ($1 - \alpha = 0.95$). Indeed, the echoes due to high-level noise in [40–50 μs] and the rebound echoes in [0–10 μs] are emphasised in Fig. 19b. Figure 20b also shows the rebound echoes in [0–10 μs] and the defect echoes in [50–65 μs]. Both Figs. 19 and 20 highlight the advantage of the change operated on the original scalogram.

Results from the application of the method to other A-scans are shown in Fig. 21. According to Fig. 2, A-scan no. 137 is expected to cross some structural noise in the base metal (area 2) and a strong raising noise (area 3). But Fig. 21 (b) shows that the noise in area 3 is not stronger than that of area 2 for this y coordinate. A-scan no. 560 and A-scan no. 623 have been chosen around A-scan no. 597. A similar flaw echo is noticed in [60–65 μs] in Fig. 21c and in [30–35 μs] in Fig. 21d. These echos, considered with that in Fig. 20b in [50–55 μs], give information which could lead to estimate the location and the size of the flaw. In addition, it is noticeable that the rebound echoes in [0–10 μs] are all represented by a similar pattern in the time-frequency representation in Figs. 19, 20, 21. It is also the case for the strong structural noise in Figs. 19b and 21c in [40–50 μs].

4.2.2 Material B

The modified scalogram of signal A-scan no. 11 (see Fig. 7), extracted from the B-scan image in Fig. 6, is represented in Fig. 22. The structural noise used in the modeling is extracted from an A-scan signal within the third area of the B-scan image (see Fig. 6) in the base metal. The modified scalogram of signal A-scan no. 102 (see Fig. 8) crossing a welding zone is given in Fig. 22.

The areas inside the contours also correspond to values of the modified scalogram $G(\tau, s)$ above 1 [Eq. (21)]. In fact,

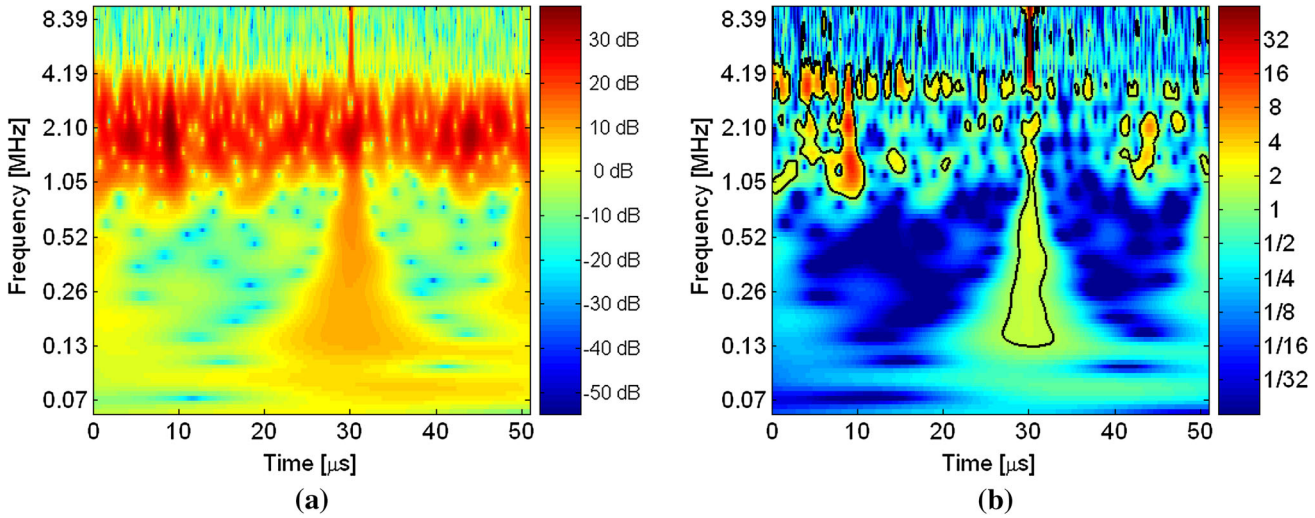

Fig. 22 Time-frequency representations of A-scan no. 11: **a** scalogram, **b** scalogram modified according to Eq. (21)

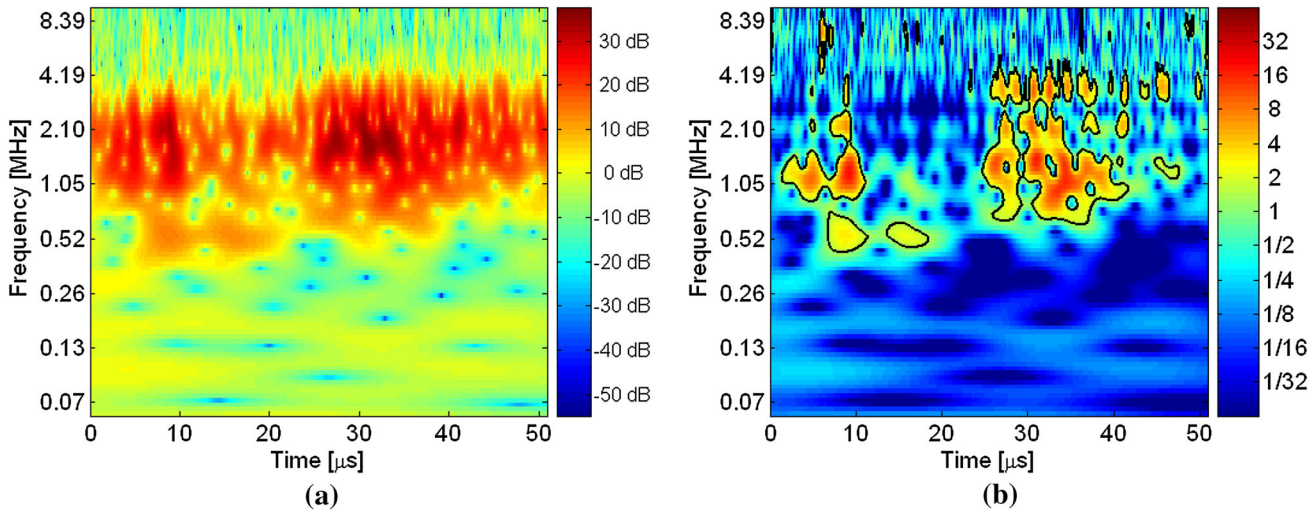

Fig. 23 Time-frequency representations of A-scan no. 102: **a** scalogram, **b** scalogram modified according to Eq. (21)

in Fig. 22 rebound echoes are visible at the beginning of the signal. In the middle of the signal, noise echoes with an amplitude level higher than the modeled noise are highlighted. In Fig. 23, in addition to the rebound echoes, the echoes due to the reflections at the bottom of the weld are found out. These echos of high amplitude emerge from the structural noise because of the roughness of the bottom of the weld, which causes numerous dispersive reflections. However it is noticeable that some echoes in the welded zone have no contour in the interval [20–25 μs]. This zone is regarded as a structural noise because it represents a very low level of noise. This is probably due to the alignment of the grains in this welded zone.

5 Conclusion

The method presented here consists first in characterizing the structural noise in austenitic stainless steels. Secondly, when flaws or welds are present in the material, using both CWT and hypothesis testing allows us to differentiate the structural noise from other echoes in the ultrasonic signal. The CWT gives a time-scale (or a time-frequency) representation which may be difficult to interpret, that is why hypothesis testing is proposed. The aim of this study is to provide a quantitative interpretation of each pattern (constituted by the amplitudes within some areas of this time-scale representation) in order

to know if these patterns correspond to structural noise or to flaws. The knowledge on the frequency content of structural noise is injected in the decision process leading to the proposition of a modified scalogram expected to emphasize echoes that are not considered as structural noise. This knowledge is provided by the autoregressive model linked to the structural noise signal.

According to the results obtained and their analysis, the approach implemented based on modeling the structural noise and on hypothesis testing in the time-scale (or time-frequency) plane, seems to be of great interest. Indeed, the method leads within an ultrasonic signal A-scan to differentiate various echoes from the structural noise. A similar study could be applied to other materials with strong structural noise such as the centrifuged cast steels and the concretes. Various kinds of structural noise could be modeled with the method and a perspective would be to recognize waveforms different from these classes of noise. The method could work on time-frequency or time-scale representations provided by another technique than the CWT. This approach could be used to consider the height of the plane defects emerging, which is based on the difference of time of flight between diffraction and corner echoes, the echoes of diffraction being often drowned within the structural noise in particular for the centrifuged cast steels.

Acknowledgements The authors wish to acknowledge the colleagues from EDF (B. Chassignole's team) for their collaboration, in particular for the experiments providing the ultrasonic signals. H. Dhifaoui is also to be thanked for his preliminary work on the subject.

References

1. Stanke, F.E., Kino, G.S.: A unified theory for elastic wave propagation in polycrystalline materials. J. Acoust. Soc. Am. **75**(3), 665–681 (1984)
2. Rose, J.H.: Ultrasonic backscattering from polycrystalline aggregates using time-domain linear response theory. Rev. Prog. Quant. Non Destr. Eval. **11**, 1677–1684 (1991)
3. Ahmed, S., Thompson, R.B.: Influence of columnar microstructure on ultrasonic backscattering. Rev. Prog. Quant. Non Destr. Eval. **14**, 1617–1624 (1995)
4. Saniie, J., Wang, T., Bilgutay, N.M.: Analysis of homomorphic processing for ultrasonic grain signal characterization. IEEE Trans. Ultrason. Ferroelectr. Freq. Control **36**(3), 365–375 (1989). doi:10.1109/58.19177
5. Kay, S.M.: Modern Spectral Estimation: Theory and Application. Prentice Hall, Englewood Cliffs (1988)
6. Schmidt, R.O.: Multiple emitter location and signal parameter estimation. IEEE Trans. Antennas Propag. **34**, 276–280 (1986)
7. Saniie, J., Jin, X.M.: Spectral analysis for ultrasonic non destructive evaluation applications using autoregressive, Prony and multiple signal classification methods. J. Acoust. Soc. Am. **100**(5), 3165–3171 (1996)
8. Mallat, S.: A Wavelet Tour of Signal Processing, 2nd edn. Academic Press, New York (1999)
9. Sharma, G.K., Kumar, A., Babu Rao, C., Jayakumar, T., Raj, B.: Short time Fourier transform analysis for understanding frequency dependent attenuation in austenitic stainless steel. NDT&E Int. **53**, 1–7 (2013). doi:10.1016/j.ndteint.2012.09.001
10. Robini, M.C., Magnin, I.E., Benoit-Cattin, H., Baskurt, A.: Two-dimensional ultrasonic flaw detection based on the wavelet packet transform. IEEE Trans. Ultrason. Ferroelectr. Freq. Control **44**(6), 1382–1394 (1997)
11. Saniie, J., Mohamed, M.A.: Ultrasonic flaw detection based on mathematical morphology. IEEE Trans. Ultrason. Ferroelectr. Freq. Control **41**, 150–160 (1994)
12. Kaya, K., Bilgutay, N.M., Murthy, R.: Flaw detection in stainless steel samples using wavelet decomposition. In: Proceedings of the IEEE Ultrasonics Symposium, pp. 1271–1274 (1994)
13. Bilgutay, N.M., Saniee, J., Furgusson, E.S., Newhouse, V.L.: Flaw-to-grain echos enhancement. In: Proceeding of the Ultrasonics International, pp. 152–157 (1979)
14. Qi, T., Xing, L., Bilgutay, N.M.: Multiple target detection using split spectrum processing and group delay moving entropy. IEEE Trans. Ultrason. Ferroelectr. Freq. Control **42**(6), 1076–1086 (1995). doi:10.1109/58.476551
15. Oruklu, E., Saniie, J.: Ultrasonic flaw detection using discrete wavelet transform for NDE applications. In: Proceedings of the IEEE Ultrasonics International, pp. 1054–1057 (2004)
16. Abbate, A., Koay, J., Frankel, J., Schroeder, S.C., Das, P.: Signal detection and noise suppression using a wavelet transform signal processor: application to ultrasonic flaw detection. IEEE Trans. Ultrason. Ferroelectr. Freq. Control **44**(1), 14–25 (1997)
17. Demirli, R., Saniie, J.: Asymmetric Gaussian Chirplet model for ultrasonic echo analysis. In: Proceedings of the IEEE Ultrasonics Symposium (IUS), 11–14 Oct 2010, pp 124-128 (2010). doi:10.1109/ultsym.2010.5935677
18. Asraf, D.E., Gustafsson, M.G.: Optimal detection of crack echo families in elastic solids. J. Acoust. Soc. Am. **113**(5), 2732–2741 (2003)
19. Saniie, J., Wang, T., Jin, X.: Performance evaluation of frequency diverse Bayesian ultrasonic flaw detection. J. Acoust. Soc. Am. **91**(4), 2034–2041 (1992)
20. Jevrejeva, S., Moore, J.C., Grinsted, A.: Influence of the Arctic Oscillation and El Niño-Southern Oscillation (ENSO) on ice conditions in the Baltic Sea: the wavelet approach. J. Geophys. Res. **108**(D21, 4677), ACL 10, 11–11 (2003)
21. Torrence, C., Compo, G.: A practical guide to Wavelet analysis. Bull. Am. Meteorol. Soc. **79**, 61–78 (1998)
22. Grinsted, A., Moore, J.C., Jevrejeva, S.: Application of the cross wavelet transform and wavelet coherence to geophysical time series. Nonlinear Process. Geophys. **11**, 561–566 (2004)
23. Chassignole, B., El Guerjouma, R., Ploix, M.A., Fouquet, T.: Ultrasonic and structural characterization of anisotropic austenitic stainless steel welds: towards a higher reliability in ultrasonic non-destructive testing. NDT&E Int. **43**, 273–282 (2010). doi:10.1016/j.ndteint.2009.12.005
24. Chassignole, B.: Influence de la structure métallurgique des soudures en acier inoxydable austénitique sur le contrôle non destructif par ultrasons [Influence of the metallurgical structure of austenitic stainless steel welds on ultrasonic nondestructive testing]. Doctoral Dissertation, Institut National des Sciences Appliquées, Lyon, France (2000)
25. Kaiser, G.: A Friendly Guide to Wavelets. Birkhäuser, Boston (1994)
26. Grinsted, A., Moore, J.C., Jevrejeva, S.: MatLab software package. http://noc.ac.uk/using-science/crosswavelet-wavelet-coherence (2016). Accessed 4 May 2016
27. Chatfield, C.: The Analysis of Time Series: An Introduction, 4th edn. Chapman and Hall, London (1989)

28. Johnson, P.E., Long, G.: The probability density of spectral estimates based on modified periodogram averages. IEEE Trans. Signal Process. **47**(5), 1255–1261 (1999)
29. Huillery, J., Milioz, F., Martin, N.: On the description of spectrogram probabilities with a Chi-Squared law. IEEE Trans. Signal Process. **56**(6), 2249–2258 (2008)
30. Shapiro, S.S., Wilk, M.B., Chen, H.J.: A comparative study of various tests for normality. J. Am. Stat. Assoc. **63**(324), 1343–1372 (1968)
31. Oppenheim, A.V., Schafer, R.W.: Discrete-Time Signal Processing. Prentice-Hall, Englewood Cliffs (1989)
32. Proakis, J.G., Manolakis, D.G.: Digital Signal Processing, Principles, Algorithms, and Applications. Prentice-Hall, Englewood Cliffs (1996)